J. Fluid Mech. (2000), *vol.* 417, *pp.* 127–156. Printed in the United Kingdom

Laboratory simulation of the rise of buoyant thermals created by open detonation

By ROGER S. THOMPSON[1], WILLIAM H. SNYDER[2]† AND JEFFREY C. WEIL[3]

[1]Atmospheric Modeling Division, National Exposure Research Laboratory, US Environmental Protection Agency, Research Triangle Park, NC 27711, USA

[2]Atmospheric Sciences Modeling Division, Air Resources Laboratory, National Oceanic and Atmospheric Administration, Research Triangle Park, NC 27711, USA

[3]Cooperative Institute for Research in Environmental Sciences, University of Colorado, Boulder, CO 80309, USA, and visiting scientist, National Center for Atmospheric Research, Boulder, CO 80307, USA

(Received 28 April 1998 and in revised form 23 March 2000)

Laboratory experiments were conducted in a water tank to investigate the rise through the atmosphere of thermals generated by the detonation of surplus military munitions. The fall of a dense volume of fluid through the water in the tank follows the same governing equations as the rise of a buoyant volume of gas in the atmosphere. By filling the tank with a layer of water and a layer of salt water, an elevated step change in density was obtained, simulating a temperature inversion or jump in the atmosphere. The growth of the linear dimensions of the thermal and its volume were determined and used in the development of a criterion for predicting when a thermal will fully penetrate the inversion. Replacing the second layer of fluid with water of gradually increasing salinity, an elevated constant density gradient was obtained. In these cases, the maximum penetration distance of the thermal was observed and the equilibrium position and vertical spread were determined experimentally.

These observations and the empirical relationships determined from them should prove useful in the development and evaluation of air pollution dispersion models for predicting the atmospheric transport and diffusion of material released during such detonations.

1. Introduction

The most common method for disposing of obsolete military munitions is by open detonation in an earthen pit. Currently, small batches of material (100 to 5000 lb) are destroyed by such means, and they leave behind buoyant thermals or clouds of contaminants. Open detonation is at present restricted to daytime when atmospheric dispersion is most rapid and generally occurs within a deep convective boundary layer (CBL) or mixed layer that is capped by a temperature inversion. An important question concerns the rise and spread of buoyant thermals and their ability to penetrate the elevated inversion, above which they would be subjected to different wind speeds and directions than in the CBL. This question and evaluation of the

† On assignment to the National Exposure Research Laboratory, U. S. Environmental Protection Agency. Present address: 7312 Grist Mill Rd., Raleigh, NC 27615-5402, USA.

effects of detonating larger quantities are being pursued by the development of new dispersion models (Weil *et al.* 1996), but a key requirement is new experimental data.

This paper reports on laboratory simulation of the rise and spread of buoyant thermals and, in particular, their inversion penetration capability. The present study provides a fundamental database and empirical descriptions of the physical processes involved for evaluation of these dispersion models.

While the ultimate goal of this effort is to understand the processes involved for a thermal rising through a convective boundary layer, these laboratory experiments were carried out at reduced scale in a quiescent tank. The scaling of the atmospheric variables followed the usual requirements (Snyder 1981). Of course, the Reynolds number of the atmospheric thermals could not be matched in the laboratory and the principal of Reynolds-number independence was applied. The dense volumes of water released in the laboratory tank generated highly turbulent *thermals* and, although their Reynolds number is much less than that in the atmosphere, the turbulent behaviour is similar. The intensity of the turbulence generated within a thermal is much greater than that of the ambient atmospheric CBL. Photographs and video recordings frequently show strongly buoyant *mushroom clouds* that rise through the atmosphere without being strongly distorted by the ambient turbulence, and this process is easily simulated in our quiescent tank. Weak thermals which rise more slowly will be more strongly affected by ambient turbulence; the current study provides the first step in understanding the physical processes involved – the rise of thermals through a non-turbulent environment. Further studies are underway in our convection tank to aid understanding of the interaction of buoyant thermals with strong ambient turbulence.

Our study progressed in phases. First, we evaluated the growth and rise of a thermal in a neutral environment. Second, we determined the fraction of the thermal that penetrated an elevated inversion (step change in density) above a neutral surface layer. Third, for thermals released into a neutral layer followed by a stratified layer with a constant density gradient, we investigated the maximum penetration height, the equilibrium height at which the thermal ceases vertical motion, and the vertical thickness at this equilibrium height. Finally, we explored how a step change in density at the base of the constant gradient region influenced the thermal. Laboratory techniques were developed for the simulation and measurement of the motion of thermals under these conditions.

Morton, Taylor & Turner (1956) and Turner (1957) were pioneers in the laboratory investigation of the rise of buoyant thermals. By injecting small volumes of buoyant fluid through an opening in the bottom of a water tank, they created buoyant thermals with substantial vertical momentum. Their thermals had significant initial circulation and thus formed highly organized vortex rings. In contrast, our thermals were released from a rotating cup with no initial vertical momentum and effectively zero initial circulation. Turner (1986) points out that 'important properties of thermals can be understood better if they are regarded as a special case of a buoyant vortex ring...'. He further explains that 'For a thermal, the circulation is generated by buoyancy, whereas in a vortex ring, the buoyancy and circulation... can be specified independently at the source'. Because of the limited influence of circulation in our study, we concentrate on the bulk properties of the thermals, expecting the only rotational effects to be those generated by the buoyancy.

Two previous experimental studies (Richards 1961 and Saunders 1962) were used as the basis for the design of the present one. A dense volume of dyed fluid was initially contained inside a hemispherical cup such that its upper surface matched the water surface in a water tank; the cup was quickly rotated, thus instantaneously

releasing a hemispherical thermal at the water surface. The negatively buoyant fluid falling through the tank models a buoyant thermal rising through the atmospheric boundary layer where variation in the tank fluid density corresponds to variations in atmospheric potential temperature. Richards photographed thermals falling through his tank; the photographs were used to determine the location and size of the thermals as functions of time. In the present study, application of video recording and computer graphic analysis greatly facilitated the data reduction.

In general, the geometric relationships of Richards (1961), Saunders (1962) and Scorer (1957) were found to represent the growth of thermals in a neutral environment as obtained in the current study. These authors reported that the horizontal dimension of a thermal is proportional to its distance from a virtual origin (the position it would have started from if it had started at a point). However, the variability in the proportionality constant in our results is much less than that of Richards.

For his step change in density experiments, Richards defined a non-dimensional parameter $S = V(\rho_2 - \rho_1)/M$ as a measure of the strength of the density change across the interface compared with the buoyancy of the thermal as it straddled the interface. V is the measured volume of the thermal when its widest span is at the level of the interface, $(\rho_2 - \rho_1)$ is the density change across the interface, and M is the excess mass of the thermal (mass of the thermal minus the mass of an equivalent volume of water from the upper layer). Richards found that the fraction of the thermal that penetrated the interface decreased linearly as S increased from 0.1 to 1.9. When using our measured volumes (obtained when the thermal centroid was at the interface), we found a similar linear dependence, but over the range in S from 1.0 to 2.9. For S less than 1.0 we observed essentially complete penetration. Richards' formulation used the measured volume of the thermal when its widest point was at the interface. We prefer to use a predictive approach and obtain an estimate for the thermal volume when the centroid is at the interface. By replacing the measured volume in Richards' formula with this predicted volume, V_p, we define a new non-dimensional parameter $\Delta = V_p(\rho_2 - \rho_1)/M$, whose value determines whether or not penetration occurs.

Thermals were also released into a neutral layer that was followed by a constant density gradient region. A neutral layer capped by a stable layer is an idealization of the CBL (Perry & Snyder 1989; Wyngaard 1988) in which most munition detonations occur. An additional feature often observed in CBL temperature profiles is a finite change in the potential temperature at the base of the inversion. As a cursory investigation of this problem, two sets of experiments were conducted with a step change in density at the base of the gradient. The thermal centroid, vertical spread or standard deviation, and the maximum distance of thermal penetration into the elevated gradient region were determined from measurements. Saunders' (1962) theory for the maximum penetration depth of a thermal released into an elevated gradient environment is modified here to include a step change in density at the base of the gradient. Observations of the maximum penetration depth compare well with these predictions. The authors are not aware of any theories for predicting either the equilibrium depth or thickness, but our data show that these quantities appear to be related to the maximum depth.

2. Experimental details

The towing tank of the Fluid Modeling Facility of the US Environmental Protection Agency was used as a saltwater stratified tank for this study (see Thompson & Snyder 1976). The tank was filled using standard techniques, typically to a depth of 108 cm.

Because our experiments were performed using falling volumes of fluid with a density greater than the surroundings, we discuss them with the vertical coordinate z measured positive downwards and using fluid density as the variable producing the buoyancy (the heavy thermal has positive buoyancy in this coordinate system). This approach is consistent with the theoretical development of Saunders (1962) which is adapted herein. When applying our results to atmospheric situations, z is positive upwards (measured from the Earth's surface) and density is replaced by potential temperature as the variable producing the thermal's buoyancy. In addition, Richards (1961) and Saunders (1962) describe the properties of a thermal as a function of the depth of its *front* or *cap*. Because of the billowy shapes of thermals, protuberances at the leading edge may increase the uncertainty in defining the front position and increase the scatter in the measurements of that position. Thus, we also use the depth of the centroid as an independent variable in characterizing the vertical position of the thermal. The centroid is directly computed by the video analysis software. However, in the presentation of the theory, we will retain Saunders' use of distance to leading edge for easy comparison with his results and because it simplifies the expressions for entrainment at an interface.

Two data reports (Thompson & Snyder 1996*a, b*) present more extensive details of the experimental setup as well as computer files containing the collected data.

2.1. *Classification of density profiles*

Neutral atmospheric conditions were simulated by filling the tank with fresh water. We refer to neutral atmospheric conditions as a *type-N* environment. To model atmospheric conditions with an elevated inversion, a dense saltwater layer was placed below a fresh water layer to create an interface with a step change in density at a specified depth; this is referred to as a *type-S* environment. For modelling an elevated gradient, *type-G* environment, the density of each layer below a neutral layer was incrementally increased to obtain the desired gradient. In one instance, a step change in density was included between the neutral layer and constant gradient; we call this a *type-SG* environment.

2.2. *Measurement of density profiles*

The technique for measuring vertical density profiles of salt water in the tank was similar to that used by Richards (1961) and Saunders (1962). An aluminium disk (9.7 cm diameter, 1.0 cm thick) was suspended in the tank on a length of monofilament fishing line attached to a stabilizing brass tube extension on top of the disk. The top end of the line was connected to an electronic balance that measured the weight of the disk. The balance, with the weight attached, was raised and lowered to programmed depths on a motor-driven platform. The entire system was computer controlled and programmed to compute the density of the fluid by comparison of the weight of the disk in the water and in air. The disk was very slowly moved between measurement positions to minimize the disturbance to the surrounding fluid. At each measurement position, the system was allowed to stabilize before recording the weight of the disk.

Examples of three density profiles measured prior to releases are shown in figure 1 for type-S, type-G, and type-SG environments. The small inadvertent jump at the base of the gradient ($z \simeq 31$ cm) in the type-G profile was typical, but was not considered to have a significant effect on the penetration process. Straight line segments were drawn through the data to obtain the interface depth and the value of the gradient. The profiles for the type-S and type-SG environment do not have perfect step-change interfaces. Mixing during filling and molecular diffusion spread the density change

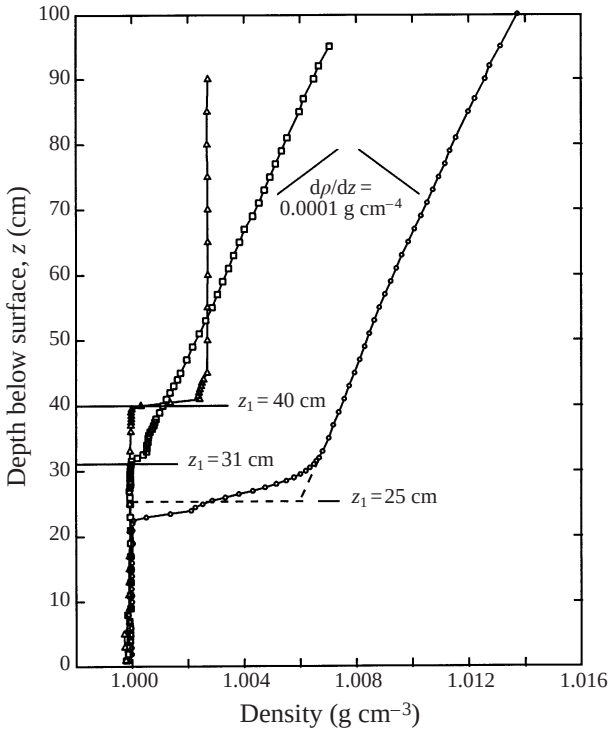

FIGURE 1. Example density profiles in the water tank to simulate various atmospheric potential temperature profiles: △, type-S environment; □, type-G environment; ○, type-SG environment.

over a few centimetres. The dashed line in the figure was the target profile for the type-SG environment and was used to define the neutral layer depth.

2.3. *Apparatus for releasing thermals*

A thin-walled stainless-steel hemispherical cup was mounted on a shaft that was rotated approximately 180° with a rotary pneumatic actuator. For each experiment, a prescribed volume (and density) of a mixture of salt water and blue food dye (typically 10% food dye by volume for the type-N and type-S experiments and 50% for the type-G and type-SG experiments) was placed in the cup. The cup was lowered into the tank until the level of the fluid in the cup matched the water level in the tank and the trailing lip of the cup was adjusted to be approximately 1 mm above the water surface. The rapid inversion of the cup resulted in a hemisphere of dyed fluid heavier than its surroundings being left at the water surface. Through early trials, we found that rotation of the cup in about $\frac{1}{15}$ s produced a repeatable initial condition, with the instantaneous appearance of a hemispherical thermal at the surface. To investigate the effect of the size and shape of the initial cloud, cups of two sizes (diameters of 7.6 and 10 cm) were mounted on shafts for easy interchange. For most releases the desired density of the mixture in the cup was obtained using sodium chloride (common salt). Solutions with density greater than $1.10\,\mathrm{g\,cm^{-3}}$ (i.e. a mass excess $M > 15\,\mathrm{g}$) and those for releases in the type-N experiments using the smaller cup were prepared using calcium chloride. The mass excess is the difference in mass of the release solution and that of an equal volume of water from the neutral layer.

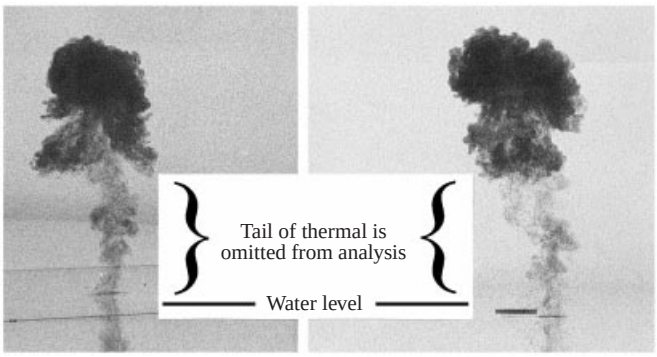

FIGURE 2. View of a thermal from the video camera. The image is inverted to provide atmospheric perspective. Front view is on the right, side view is on the left.

2.4. *Experiments in type-N and type-S environments*

The motion of the thermals was recorded on videotape with a camera positioned to obtain simultaneous front and side views of the thermals. A frontal or direct view was obtained in the usual manner, with the camera viewing the thermal against a translucent panel illuminated from the back. A large mirror was placed to one side of the thermal path at nominally 45° to the camera-view axis to obtain a simultaneous side view of the thermal. The mirror was adjusted to reflect a view perpendicular to the direct one and a second mirror was positioned to obtain a lighted background (as for the direct view). Figure 2 shows a snapshot view from the video camera (inverted to provide an atmospheric perspective) of a thermal in the tank. The camera signal was routed through a time-marking device that added the time to each video frame.

A three-dimensional wire frame (two 25 cm squares in perpendicular vertical planes) was suspended in the water with its top level with the water surface; this frame was used to align the camera and mirrors. Prior to each series of experiments, a short recording of the frame was made and used to define and scale the coordinate system during the digital analysis of the thermal trajectories and shapes.

The video analysis procedure was as follows. The videotaped recording of each experiment was copied onto an optical disk for random access and frame-grabbing by a personal computer. Time $t = 0$ was taken as the time of the first frame after the cup had rotated out of view. This frame as well as ten at later times were grabbed for each thermal released and stored as TIFF (Tagged Image File Format) files; duplicates were made to provide one set for front-view and another set for side-view analysis. These TIFF files were individually loaded into a video analysis program that displayed them on the monitor; outlines of the thermals were traced by the program under the operator's supervision. In particular, the small tail of dye left behind by the falling thermal was omitted by directing the trace across the thermal's trailing edge at the operator's discretion (see figure 2).

The program automatically determined several geometric parameters of the thermals, including area, coordinates of the top and bottom, coordinates of the extreme lateral boundaries, and location of the centroids. These values were transferred to a spreadsheet file using direct data entry, wherein additional parameters were computed. Using this information for each front and side view, we averaged the pairs of values to determine the depths of the leading edge and centroid.

An estimate of the volume of each thermal was made by assuming that its shape could be approximated by an oblate spheroid with volume $(4/3)\pi(D/2)^2(H/2)$, where

D is the major axis (lateral dimension) and H is the minor axis (vertical dimension) of the thermal. Because the front-and side-view images differ slightly, this is rewritten using the front-view area A_f, side-view area A_s and average vertical dimension D_V to obtain $V = (8A_fA_s)/(3\pi D_V)$. Thus, estimates of the volumes of the thermals were based on dimensions obtained directly from the video analysis. Of course, if the thermal's shape were a perfect spheroid, the volume computed in this manner would be exact. As a demonstration of the error incurred if the thermal were not a spheroid, we can apply the formula to a shape quite different from a spheroid, say, a cube with faces perpendicular to the viewing axes; this formula estimates the volume to be only 15% too low. Because the shapes of our thermals are, in general, much closer to oblate spheroids, we expect the errors involved to be much less than 15%. Richards (1961) used an integration approach to compute the volume; the procedure involved dividing the thermals into horizontal slices, determining the front- and side-view dimensions of each slice, and integrating the estimated areas of slices over the vertical dimension of the thermal. His formula was based on the assumption that horizontal slices of the thermal are elliptical, which seems to be quite similar to our approach in that the thermal is a spheroid. Using Richards' technique on three arbitrary front- and side-view pairs of thermals resulted in video-analysis volumes 6%, 12%, and −7.5% larger than the volume determined using our method. Considering the degree of operator discretion involved in both methods, these rather small differences suggest that the methods produce equivalent results.

We use the terms *penetration* to denote the thermal mass that passes through the interface and *penetration depth* to denote the maximum depth that the thermal leading edge attains. Our estimates of penetration were made by reviewing the video record and estimating the fraction of each thermal's mass that passed through the interface. For discussion purposes, we assume rapid mixing inside the thermal, so that the density inside the visible boundary is uniform. The density of a thermal decreases as it entrains fluid in the neutral upper layer. If, after passing through the interface, the thermal density is greater than that of the surroundings, it will continue to fall, with essentially total penetration and infinite penetration depth. If the density is less than that of the surroundings, the thermal will reverse direction and return to the interface. Estimating the penetration from observations of thermals with small or large density differences was rather easy. However, for intermediate cases, the estimation was sometimes difficult. Typically, for the intermediate cases, some portion of the thermal initially passed through the interface and, depending on the momentum and buoyancy, that portion (i) reversed direction and returned to the interface, (ii) continued on to some lower position, or (iii) stagnated. In some cases, the portion penetrating the interface was observed to divide, with a portion returning to the interface and the remainder continuing to fall. With this in mind, an *initial penetration* P_i was defined as the fraction of the thermal that initially passed through the interface as an identifiable mass. A *final penetration* P_f was defined as the fraction of the thermal that ultimately continued to fall. Of course, for weak and for strong thermals, the initial and final values were the same, 0 and 90% to 100%, respectively. (Even strong thermals lost 5% to 10% of their initial mass to the residual tail that remained in the upper layer.) The initial and the final penetration values (estimated to the nearest 5%) were obtained for all type-S experiments from analysis of the video record.

2.5. *Experiments in type-G and type-SG environments*

Elevated atmospheric temperature gradients were simulated by filling the tank with layers of increasing (with depth) density below a neutral layer of essentially fresh

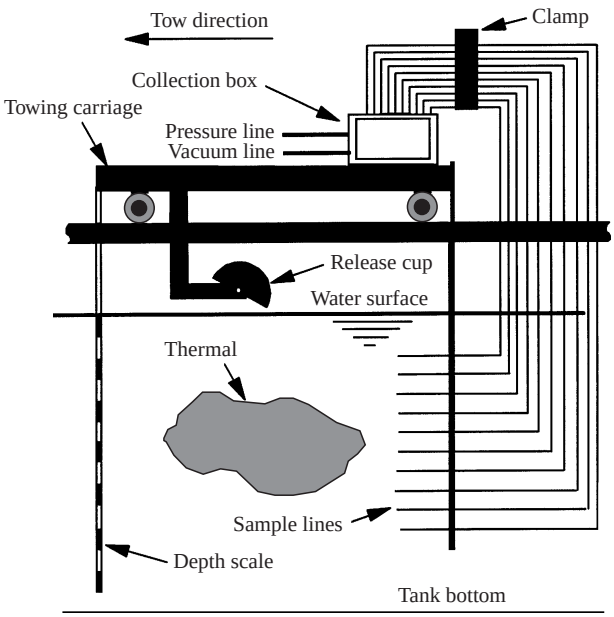

FIGURE 3. Schematic of the system for sampling thermals at the equilibrium height.

water. Sets of up to eight repetitions of a given experiment were conducted by moving the release mechanism to different positions along the tank. By quickly moving the apparatus to a neighbouring position, an additional release was made before the dye from previous releases spread into view. The careful alignment of the video camera system required to obtain recording for video analysis of each release was not practical. Therefore, to determine the penetration depth of thermals, a small diameter gridded rod was suspended in the tank. The rod was placed well to the side of the release cup to minimize interference with the thermals. For each release, an observer would estimate the thermal penetration depth (to the nearest 5 cm) by sighting against this rod.

A support for positioning a 10×10 array of sampling ports was attached to a towing carriage such that the array could be moved through the dyed fluid as soon as the thermal reached its equilibrium depth. A schematic of the sampling apparatus is shown in figure 3. Both the vertical and horizontal spacings of the rake were adjustable and set before each series of releases with the goal of just spanning the width and the vertical thickness of the thermal. The uniform vertical and horizontal spacings varied from 2 to 8 cm and 10 to 15 cm, respectively.

Each of the 100 sample ports was connected to an outlet port above a test tube within a collection box. The sampling protocol was as follows. A rack of empty test tubes was placed in the collection box. The box was sealed and pressurized to flush out any residual fluid from the lines. A clamp closed off the sample lines and the rake was lowered into the tank to a predetermined depth. A vacuum pump created suction in the collection box. A thermal was released and observed until it had fallen to its maximum depth, reversed its direction and reached an *equilibrium* depth, at which time the towing carriage moved the rake through the thermal. The clamp was released to initiate sampling just before the rake reached the thermal. After the rake had passed completely through the thermal and the test tubes were full, the clamp was reapplied to stop the sampling. The distance the sample rake travelled while the test

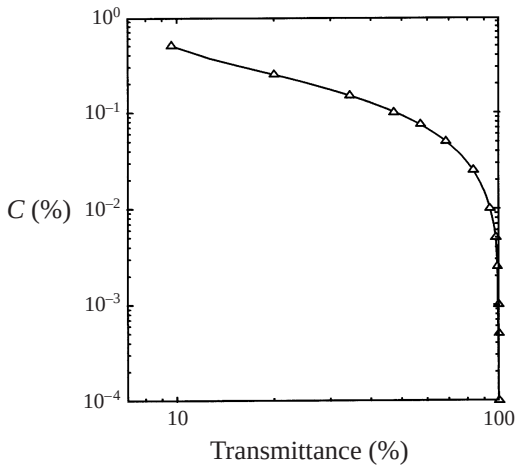

FIGURE 4. Typical calibration curve for the colorimeter used for obtaining the dye concentration of samples collected during the experiments.

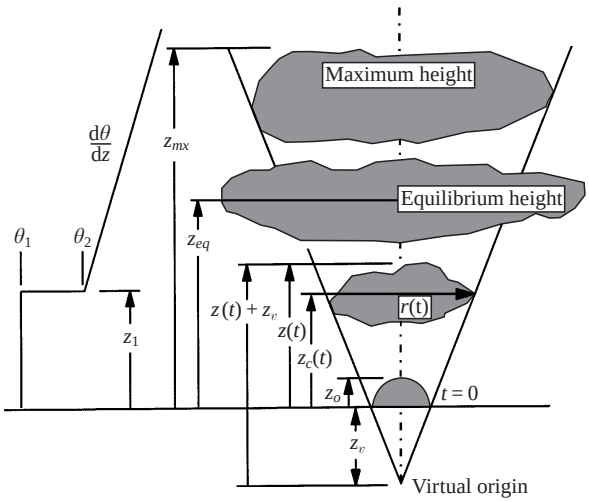

FIGURE 5. Variables to describe the rise of a buoyant thermal in the atmosphere. Invert the figure and replace θ with ρ for water tank experiments.

tubes were being filled was measured and recorded. The volume of fluid represented by the sample was computed by multiplying this travel distance by the vertical and the horizontal spacing of the sample rake.

The light transmittance of the sample in each test tube was measured with a Brinkman (model PC800) colorimeter connected to a personal computer for data acquisition. A hand-held light probe was inserted into the fluid in each test tube, and the output was sampled by computer. The colorimeter was calibrated (to convert transmittance to concentration of dye) using carefully prepared known dilutions of a source mixture. A typical calibration curve consisting of best-fit piecewise Beer's-law formulas is shown in figure 4. Concentrations of samples from ports that intersected the thermal were typically between 0.01% and 0.25%, falling within a region of the calibration curve that provided good resolution.

3. Theoretical considerations

The descriptive variables for a thermal moving through a type-SG environment are shown in figure 5. The motion of a thermal in type-N, type-S, and type-G environments may be considered as special cases of this more general situation. A thermal entering the constant gradient region attains a limiting or maximum height where it stops; the height of the leading edge at this point is called z_{mx}. The thermal then moves back toward the interface and comes to rest with its centroid at an equilibrium height z_{eq}.

Richards (1961) and Scorer (1957) expressed the observed linear growth of thermals with height (in non-stratified surroundings) as $z = n_1 r$, where z is the depth of the front of the thermal and r is the lateral radius (see figure 5). We use this expression, but explicitly include the virtual origin, i.e. $(z + z_v) = n_1 r$. We also use the depth of the centroid z_c which is related to the radius as $(z_c + z_v) = n_c r$. Given that the radius grows linearly with height, we may expect that the vertical dimension of the thermal does also. This leads to the expectation that the volume of the thermal is $V = \beta(z + z_v)^3 = \beta_c(z_c + z_v)^3$, where β and β_c are constants. The values for n_1 and n_c varied from thermal to thermal, and we will use ensemble average values of β, and β_c to predict the growth.

Saunders (1962) derived and solved equations to describe the motion of a thermal as a function of time t through type-N, type-S, and type-G environments. He made simplifying assumptions about the entrainment of ambient fluid into the thermal in order to solve the equations. His approach and nomenclature will be generally followed here in solving the more general case consisting of a type-SG environment, from which Saunders' solutions can be obtained.

As presented by Saunders (1962), the governing equations for the mean motion of a thermal, expressed in terms of its volume-averaged or bulk properties, are as follows:

momentum

$$W\frac{\mathrm{d}}{\mathrm{d}z}(\alpha V W) = g\overline{B}V, \tag{3.1}$$

buoyancy

$$\frac{\mathrm{d}}{\mathrm{d}z}(g\overline{B}V) = -\frac{Vg}{\rho_1}\frac{\mathrm{d}\overline{\rho}_E}{\mathrm{d}z}, \tag{3.2}$$

mixing

$$V = \beta(z + z_v)^3, \tag{3.3}$$

where W is the vertical velocity of the cap of the thermal, V the volume of the thermal, $\overline{\rho}_E$ the volume average density of the fluid displaced by the thermal at depth z, ρ_1 the reference density (neutral layer), $\overline{\rho}$ the mean density of the thermal, $\overline{B}$ the density excess of thermal, $(\overline{\rho} - \overline{\rho}_E)/\rho_1$, α the virtual mass coefficient, dimensionless, z the depth of leading edge below water surface and, z_v the distance of virtual origin above the surface.

The momentum equation is obtained from $\mathrm{d}(\alpha\overline{\rho}W\overline{V})/\mathrm{d}t = g\overline{B}_1\rho_1 V$ using a Boussinesq-type approximation $\overline{\rho} \approx \rho_1$, except in the buoyancy term, and $\mathrm{d}/\mathrm{d}t = W\,\mathrm{d}/\mathrm{d}z$. The buoyancy equation is derived from a conservation relation $\mathrm{d}(\overline{\rho}V)/\mathrm{d}z = \overline{\rho}'_E\mathrm{d}V/\mathrm{d}z$, where $\overline{\rho}'_E$ is the average density of fluid entrained at depth z and $\overline{\rho}'_E \approx \overline{\rho}_E$. The mixing equation is an empirical expression for the thermal volume, where we have explicitly included the virtual origin. Saunders (1962) points out that the mixing equation can be readily shown to be a direct consequence of the mixing law of

Morton *et al.* (1956) that the rate of entrainment of exterior fluid into a thermal is proportional to its surface area and rate of advance.

These equations can be expressed in atmospheric variables by replacing density with potential temperature θ and reversing the sign of the vertical coordinate; in particular, $\overline{B} = (\overline{\theta} - \overline{\theta}_E)/\theta_1$, and $(1/\rho_1)(\mathrm{d}\overline{\rho}_E/\mathrm{d}z) = (1/\theta_1)/(\mathrm{d}\overline{\theta}_E/\mathrm{d}z)$.

For an entrainment expression, Saunders (1962) assumed that $\overline{\rho}'_E = \overline{\rho}_E$ and suggested that $\overline{\rho}_E$ be approximated by the ambient density linearly averaged over the vertical thickness of the thermal. An error in his expression for the entrainment at a step change (the second part of his equation 8 should be $\mathrm{d}\overline{\rho}_E/\mathrm{d}z = ((\rho_2 - \rho_1)/l)(z_1/z^2)$) is corrected here. For a step change in density of $\rho_2 - \rho_1$ at the interface ($z = z_1$) and a gradient of $\mathrm{d}\rho/\mathrm{d}z = N^2\rho_1/g$ beyond, we may show that

$$\mathrm{d}\overline{\rho}_E/\mathrm{d}z = \begin{cases} 0, & 0 < z < z_1 \\ ((\rho_2 - \rho_1)/l)((z_1 + z_v)/(z + z_v)^2) & \\ \quad +(N^2\rho_1/2lg)(1 - (z_1 + z_v)^2/(z + z_v)^2), & z_1 \leqslant z \leqslant z_2 \\ (N^2\rho_1/g)((1 - (l/2)), & z_2 < z, \end{cases} \tag{3.4}$$

where $l = D_V/(z + z_v)$, D_V is the vertical dimension of the thermal, and $N = [(g/\rho_1)(\mathrm{d}\rho/\mathrm{d}z)]^{-1/2}$ is the Brunt–Väisälä frequency.

Note that the three regions of equation (3.4) correspond to the thermal (i) being entirely in the neutral layer, (ii) straddling the interface, or (iii) being entirely in the gradient layer. And, z_2 is the height of the leading edge of the thermal when its trailing edge is just touching the interface. From the definition of l, it follows that $(z_2 + z_v) = (z_1 + z_v)/(1 - l)$. Using Saunders' notation, we define a non-dimensional height $\zeta = (z + z_v)/(z_1 + z_v)$, the non-dimensional height when the thermal has just moved through the interface $\mu = (z_2 + z_v)/(z_1 + z_v) = 1/(1 - l)$, and $\zeta_p = (z_{mx} + z_v)/(z_1 + z_v)$, the normalized maximum depth reached by the thermal. The density gradient and step change in density at the interface are non-dimensionalized as $\gamma' = N^2(z_1 + z_v)/(2lg\overline{B}_1) = (z_1 + z_v)(\mathrm{d}\rho/\mathrm{d}z)V_1/(2lM)$ and $\gamma = (\rho_2 - \rho_1)/(2lg\rho_1\overline{B}_1) = (\rho_2 - \rho_1)V_1/(2lM)$, respectively. Here, V_1 is the volume of the thermal when its leading edge first touches the interface, $\overline{B}_1$ is the corresponding value of $\overline{B}$, and M is the mass excess of the thermal while in the neutral layer. Note that the definition of γ is slightly different from Saunders', because of the correction to the term for entrainment at the step change. In terms of atmospheric variables, $\gamma = [V_1(\theta_2 - \theta_1)]/[2lV_o(\theta_o - \theta_1)]$, where θ_o and V_o are the initial potential temperature and volume of the thermal, respectively, and $\gamma' = [(z_1 + z_v)/2l](\mathrm{d}\theta/\mathrm{d}z)V_1/[V_o(\theta_o - \theta_1)]$.

3.1. *Neutral layer (type-N environment)*

Given a thermal with initial volume V_o, density ρ_o, and velocity W_o, with the leading edge at a depth z_o below the water surface at time $t = 0$, equations (3.1)–(3.3) can be solved for a thermal in a neutral environment. Equation (3.2) is used to show that $g\overline{B}V$ is a constant. Then, the expression for volume (equation (3.3)) is substituted into equation (3.1) to give a first-order linear differential equation that is easily solved to give

$$W^2 = \frac{g(\rho_0 - \rho_1)V_0}{2\alpha\beta\rho_1(z + z_v)^2}\left(1 - \frac{(z_0 + z_v)^4}{(z + z_v)^4}\right) + W_0^2\frac{(z_0 + z_v)^6}{(z + z_v)^6} \tag{3.5}$$

and

$$z = -z_v + \left[(z_0 + z_v)^4 + 4W_0(z_0 + z_v)^3 t + 2\left(\frac{g(\rho_0 - \rho_1)V_0}{\alpha\beta\rho_1}\right)t^2\right]^{1/4}. \tag{3.6}$$

3.2. *Type-S environment*

Using the criterion that the thermal remain buoyant after passing through a step change in density, an analytical expression may be obtained for determining when infinite penetration height occurs. Setting the density gradient in equation (3.4) to zero, substituting the result into equation (3.2) and integrating we find an equation for the buoyancy of the thermal

$$\rho_1 g\overline{B}V = \begin{cases} \rho_1 g\overline{B}_1 V_1, & z_v < z < z_1 \\ \rho_1 g\overline{B}_1 V_1[1-\gamma(\zeta^2-1)], & z_1 \leqslant z \leqslant z_2 \\ \rho_1 g\overline{B}_1 V_1[1-\gamma(\mu^2-1)], & z_2 < z. \end{cases} \tag{3.7}$$

As Saunders (1962) pointed out, total penetration occurs if the thermal has positive buoyancy after it has moved completely into the $z > z_2$ layer, which occurs if $\gamma(\mu^2-1) < 1$. Our experimentally determined parameters will be combined with this condition to obtain a prediction of when total penetration occurs based upon initial conditions of the thermal and environment.

3.3. *Type-SG environment*

The equation for the penetration depth of the leading edge is conditional upon whether or not the thermal completely penetrates the interface before coming to rest. Equations (3.1)–(3.3) are solved, as outlined above for a neutral environment, for the three domains defined by equation (3.4). Additional constraints are matching V and $\overline{B}_1$ at z_1 and z_2. If the thermal comes to rest before the trailing edge reaches the interface, the equation for ζ_p is

$$\zeta_p^4 - \frac{\gamma'}{24}(3\zeta_p^8 - 8\zeta_p^6 + 6\zeta_p^4 - 1) - \frac{\gamma}{6}(4\zeta_p^6 - 6\zeta_p^4 + 2) = 0, \quad \zeta_p \leqslant \mu. \tag{3.8}$$

And, if the thermal moves completely into the gradient layer, the equation is

$$\zeta_p^4 - \frac{\gamma'}{24}(3\mu^8 - 8\mu^6 + 6\mu^4 - 1) - \frac{\gamma'}{4}(\zeta_p^4 - \mu^4)(\mu^4 - 1)^2 - \frac{l(2-l)\gamma'}{8}(\zeta_p^4 - \mu^4)^2$$
$$-\frac{\gamma}{6}(4\mu^6 - 6\mu^4 + 2) - \frac{\gamma}{4}(\zeta_p^4 - \mu^4)(\mu^2 - 1) = 0, \quad \zeta_p \geqslant \mu. \tag{3.9}$$

If γ is set to zero (no step change between the neutral and gradient layers), (3.8) and (3.9) reduce to Saunders' equation 24.

Equation (3.8) cannot be solved explicitly for ζ_p as a function of γ and γ', but by choosing values for two of the variables, say ζ_p and γ', the associated value of the third, γ, may be found. By repeating for additional values, a graphical representation may be obtained.

Equation (3.9) can be solved by rewriting it as a quadratic in $(\zeta_p^4 - \mu^4)$ and applying the quadratic formula. This gives

$$z_{mx} + z_v = \left[\mu^4 + \left(\frac{-B \pm (B^2 - 4AC)^{1/2}}{2A}\right)\right]^{1/4}(z_1 + z_v), \tag{3.10}$$

where $A = -l(2-l)\gamma'/8$, $B = 1 - (\gamma'/4)(\mu^2-1)^2 - (\gamma/4)(\mu^2-1)$, and $C = \mu^4 - (\gamma'/24)(3\mu^8 - 8\mu^6 + 6\mu^4 - 1) - (\gamma/6)(4\mu^6 - 6\mu^4 + 2)$.

From dimensional analysis, a parameter to characterize the buoyancy of a thermal relative to the strength of an elevated gradient in the atmosphere may be defined as $P_T = F_T^{1/4}/[(z_1 + z_v)N^{1/2}]$, where $F_T = V_o g(\rho_1 - \rho_o)/\rho_1 = Mg/\rho_1$, the buoyancy of the

Data set	Number of releases	Cup diameter (cm)	Release volume (cm^3)	$\overline{n}_c$	σ_{n_c}	$\sigma_{n_c}/\overline{n}_c$	$\overline{n}_1$	σ_{n_1}	$\sigma_{n_1}/\overline{n}_1$
Group 1	16	10	150	3.43	0.46	0.13	4.15	0.46	0.11
Group 2	8	7.6	50	4.61	0.36	0.08	5.23	0.36	0.07
Group 3	8	10	50	3.46	0.51	0.15	4.04	0.53	0.13
Scorer (1957)	18	15.2	500 (estimated)				3.84	0.68	0.18

TABLE 1. Linear growth rates of thermals for type-N experiments.

thermal in the neutral layer. P_T is related to γ' as follows:

$$P_T = \frac{F_T^{1/4}}{(z_1 + z_v)N^{1/2}} = \left[\frac{M}{(z_1 + z_v)(\mathrm{d}\rho/\mathrm{d}z)}\right]^{1/4}$$

$$= \left[\frac{[V_1/(z_1 + z_v)^3]/2l}{(\mathrm{d}\rho/\mathrm{d}z)V_1(z_1 + z_v)/2lM}\right]^{1/4} = \frac{[V_1/[2l(z_1 + z_v)^3]]^{1/4}}{\gamma'^{1/4}} \tag{3.11}$$

$[V_1/[2l(z_1 + z_v)^3]^{1/4}$ is a constant that will be determined. Henceforth, we will use P_T rather than γ' as the measure of the initial buoyancy of the thermal relative to the elevated gradient to make application of our results to the atmosphere more straightforward.

4. Results

The results of the neutral (type-N) experiments will be presented first to demonstrate the inherent variability (as expected for turbulent processes) in the growth of thermals. Next, we present the results of the step-change environment (type-S) experiments which are used to better define the growth rates of the thermal dimensions and volumes while in a neutral layer and to establish a formula for the fraction P_f of a thermal that penetrates an elevated density jump. Finally, observations of the maximum penetration depth, the equilibrium height, and thickness at the equilibrium position of a thermal that encounters an elevated gradient (type-G) environment are presented. This final section includes two cases with a step change in density at the base of the elevated gradient (type-SG).

4.1. *Type-N environment*

The tank was filled with fresh water to create a neutral environment. A total of 32 releases was made in three groups comprising two cup sizes and two release volumes. All had nominal mass excesses of 15 g above the mass of water displaced (150 or 50 g). Table 1 summarizes the details of the three groups of releases. In addition, we include results from Scorer's (1957) experiments which were conducted with a 15.2 cm diameter cup and a water depth of 107 cm (cf. 108 cm in the current experiments).

A graph of the front- and side-view dimensions versus the depth of the centroid was made for each of these releases and used to determine the virtual origin and the growth coefficient n_c from a hand-drawn line through the data. An example of such a plot for a release from the first group is shown in figure 6. Similar procedures were followed using the depth of the leading edge to determine n_1. As observed by Scorer

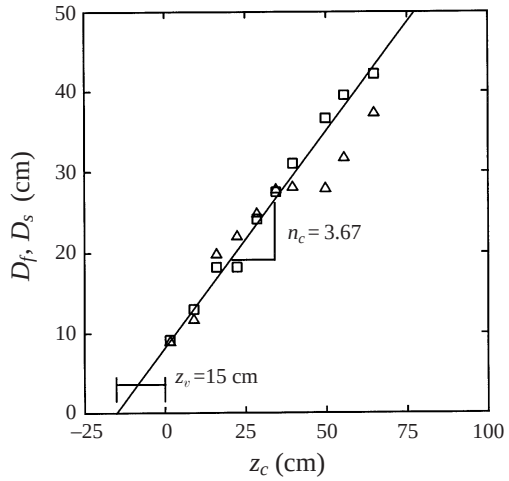

FIGURE 6. Maximum horizontal dimensions versus depth of centroid for a typical type-N experiment: △, front view; □, side view.

(1957) and Richards (1961), each thermal was observed to have a constant n_1 (and n_c) while passing through the neutral layer. The inherent variability in the falling turbulent thermals manifests itself in the strong differences observed in the values of n_1 and n_c from thermal to thermal. The mean values of the coefficients ($\overline{n}_c$ and $\overline{n}_1$), their standard deviations (σ_{n_c} and σ_{n_1}) and the ratios of the standard deviations to the means are shown in table 1 for each of the three groups. The variability in these coefficients, expressed as the ratio of the standard deviation to the mean, is seen to range from 7% to 15% for both n_1 and n_c in each of the three groups; the variability in n_1 is somewhat less than that observed by Scorer (1957). An expression for the thermal volume as a function of depth will be discussed later in conjunction with the results for the type-S environment.

The two groups of releases (1 and 3) from the 10 cm diameter cup had different volumes (and densities) of material released. The mean values of both n_c and n_1 for these groups were essentially the same. This suggests that the growth rate is independent of the release volume. The thermals released in group 2 (smaller cup, but same volume as group 3), however, resulted in somewhat larger values of $\overline{n}_c$ and $\overline{n}_1$, that is, a smaller lateral dimension at a given height than for groups 1 and 3. The first and second groups have nearly equivalent initial geometric shapes (close to a hemisphere, but slightly truncated), while the shape for the third group is much thinner in the vertical dimension. The parameter in common for the first and third groups is the cup diameter. From these limited experiments, we speculate that the initial radius of curvature of the thermal's leading edge, as determined by the cup diameter, influences the growth rate much more than the initial vertical thickness.† Scorer's (1957) result is consistent with the trend of the current data (table 1) in that his $\overline{n}_1$ and cup diameter are less than and greater than those in groups 1 and 3, respectively. Additional experiments would be required to better resolve the specific influences of cup radius and initial fluid geometry on $\overline{n}_1$ and $\overline{n}_c$.

Obtaining large mass-excess values required use of the larger release cup (10 cm dia.) with a release volume of 150 cm^3. Thus, the large cup and 150 cm^3 volumes were

† A reviewer wondered 'if the variation of n_1 on cup size seen in the current results can be attributed to possible variations in circulation generated during the development of the thermal'.

Case no.	z_i (cm)	$\rho_2 - \rho_1$ (gl^{-1})	M (g)	Leading edge z_v (cm)	n_1	n_2	Centroid z_v (cm)	n_c	P_i	P_f
1	28.5	2.60	15.3	20	5.45		20	4.29	0.95	0.90
2	28.5	2.70	15.3	25	6.25		20	4.80	0.95	0.90
3	28.5	2.70	15.3	20	5.45		20	4.44	0.95	0.90
4	28.5	2.70	15.3	25	6.25	3.33	20	4.53	0.95	0.90
5	28.0	2.60	4.50	20	5.45	2.6	15	4.26	0.50	0
19	39.0	2.30	20.1	15	3.90		15	3.33	0.95	0.90
20	39.0	2.30	17.9	15	4.79	1.93	14	3.50	0.95	0.90
65	32.5	2.15	9.87	20	5.71		20	4.62	0.95	0.90
66	32.5	2.15	9.87	15	3.97	100	15	3.00	0.50	0.30
67	32.5	2.15	9.87	18	4.45	2.67	15	3.33	0.85	0.15

TABLE 2. Samples of initial conditions and measured growth rates for type-S experiments. A complete table showing all cases is available from the JFM Editorial Office.

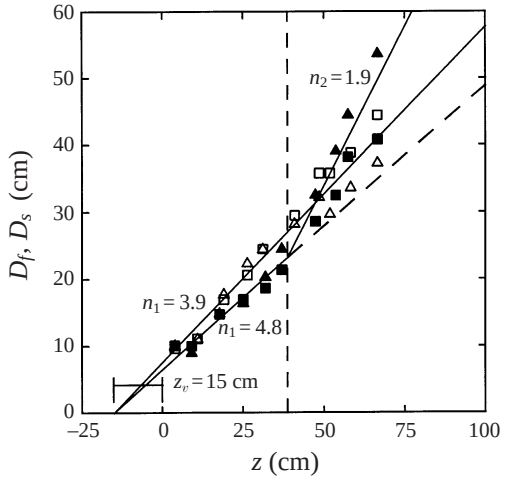

FIGURE 7. Maximum horizontal dimensions versus depth of leading edge for two type-S experiments. Case 19: △, front-view; □, side-view. Case 20: ▲, front-view; ■, side-view.

used for the remaining experiments, and the mass excess was varied by adjusting the density of the released liquid. The release shapes are, thus, roughly hemispherical.

4.2. *Type-S environments*

Table 2 shows the initial conditions for the 67 releases that were made into type-S environments, some of the results obtained from the video analysis, and the observed initial fraction of penetration P_i and final fraction of penetration P_f. The growth of each thermal's horizontal dimension was plotted for each of the cases, as a function of z and as a function of z_c. The growth coefficients n_1 and n_c were determined from the slopes of hand-drawn lines through the data in the neutral layer prior to the thermal reaching the interface. In somewhat less than half the cases, the lateral growth rate changed at the interface. This change may be expressed as a change in the growth coefficient from n_1 to n_2. If such a change occurred, usually for weak thermals, the new rate n_2 was included in table 2 to the right of the value of n_1. For weak thermals with little mass penetration, this change in growth rate is less meaningful

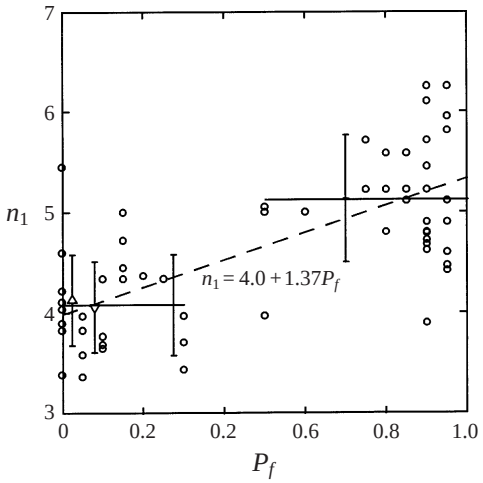

FIGURE 8. Horizontal growth coefficient versus penetration fraction for type-S experiments and mean horizontal growth coefficients for type-N experiments. Type-S: ○, individual cases; —, mean value. Type-N mean: △, group 1; ▽, group 3. Dashed line is a least-squares fit to data. Error bars are $\pm\sigma_n$.

Cases	$\overline{n}_1$	σ_{n_1}	$\sigma_{n_1}/\overline{n}_1$	$\overline{n}_c$	σ_{n_c}	$\sigma_{n_c}/\overline{n}_c$
All	4.73	0.75	0.16	3.57	0.74	0.21
$P_f < 0.5$	4.07	0.5	0.12	2.95	0.54	0.18
$P_f \geqslant 0.5$	5.15	0.56	0.11	3.97	0.57	0.14
Richards (1961)	3.96	1.27	0.32			

TABLE 3. Summary of statistics of thermals in the neutral layer.

than for cases with greater penetration. Figure 7 shows the growth of the front- and side-view dimensions of thermals as a function of the depth of the leading edge for two ostensibly identical releases, both with a final penetration of 0.9. In addition to showing the variability in n_1, one of the cases (no. 20) exhibits a sharp increase in the lateral growth rate after passing the interface, from $n_1 = 4.8$ to $n_2 = 1.9$.

Figure 8 presents n_1 versus P_f for all of the type-S experiments and suggests that n_1 separates into two distinct groups: low $P_f(< 0.5)$ cases or weak thermals and high $P_f(\geqslant 0.5)$ cases or strong thermals. Based on this separation, we have computed $\overline{n}_1$ and σ_{n_1}, for each group as well as over all cases (table 3). Figure 8 shows that $\overline{n}_1 \pm \sigma_{n_1}$ for one group overlaps little with the other and the $\overline{n}_1$ and σ_{n_1} for the low-P_f group are consistent with the values for the type-N experiments with the 10 cm diameter cup (table 1, groups 1 and 3; see also figure 8). In addition, table 3 gives the statistics for n_c and shows that $\overline{n}_c$ for the two subgroups are distinct; they differ by about $2\sigma_{n_c}$.

The separation into two P_f groups could be due in part to an overall scarcity of data and in particular for the interval $0.3 \leqslant P_f \leqslant 0.7$. An alternative interpretation of figure 8 is that n_1 varies linearly with P_f as suggested by the dashed line, which is a least-squares fit to the data. However, given the data scatter and paucity over the entire P_f range and to simplify the following analyses, we divide the n_1, thermal volume, and other properties into the low- and high-P_f groups.

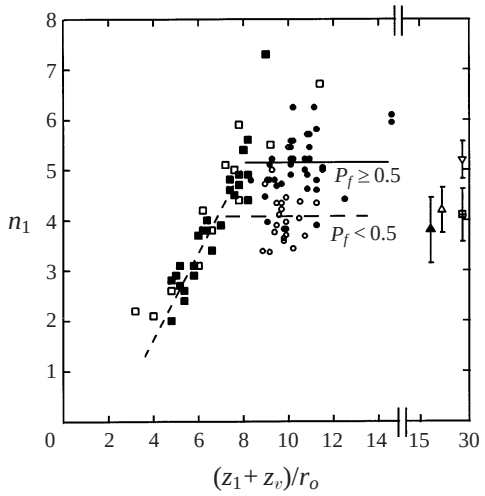

FIGURE 9. Horizontal growth coefficient versus ratio of interface depth to initial radius for type-S and type-N environments. For type-N, z_1 is fresh water depth. Type-S, Richards (1961): ■, strong thermals; □, weak thermals. Type-S, current work: ○, $P_f < 0.5$, •, $P_f \geqslant 0.5$. Type-N, Scorer (1957): ▲, $(z_1 + z_y)/r_o = 18$. Type-N, current work: △, Group 1, $(z_1 + z_v)/r_o = 22$; ▽, Group 2, $(z_1 + z_v)/r_o = 28$; ⊞, Group 3, $(z_1 + z_v)/r_o = 28$.

Table 3 also presents the n_1 statistics for Richards' (1961) experiments, which were conducted with a 10 cm diameter cup and a variable initial volume. His data, which include both strong and weak thermals, yield an $\overline{n}_1$ lower than our overall mean (4.73) and closer to the $\overline{n}_1$ for the low-P_f group. However, close inspection of Richards' data suggests that his results were influenced by a rather small ratio of interfacial depth, $z_1 + z_v$, to the initial radius r_o as discussed below.

Figure 9 is a plot of n_1 versus $(z_1 + z_v)/r_o$ for all data sets and displays three features. First, Richards' n_1 (squares) exhibit a correlation with $(z_1 + z_v)/r_o$ over the range $3 \lesssim (z_1 + z_v)/r_o \lesssim 8$ with no discernible difference between his strong and weak thermals. The correlation is attributed to an insufficient depth for the thermal to fall freely and establish its circulation pattern (e.g. see Saunders 1962) before the latter is affected by the density interface (at z_1). Second, our n_1 for strong thermals (closed circles) is consistent with Richards' data near $(z_1 + z_v)/r_o \sim 8$ and exhibits no significant trend over the range $8 \lesssim (z_1 + z_v)/r_o \lesssim 14$. Third, our n_1 for weak thermals ($P_f < 0.5$, open circles) exhibits no trend for $8 \lesssim (z_1 + z_v)/r_o \lesssim 12$ and has a mean (dashed line) consistent with Scorer's (1957) data and the neutral tank data (groups 1 and 3; table 1). The consistency of the $\overline{n}_1$ for the low-P_f cases with the latter data sets, which had large $(z_1 + z_v)/r_o$ ratios (18–25), suggests that $\overline{n}_1$ was independent of $(z_1 + z_v)/r_o$ in our experiments.

In the following, we estimate the thermal's volume from equation (3.3) by introducing a mean distance from the surface to the virtual origin, z_v. In principle, z_v should be the same whether inferred from the leading edge or centroid position. We determined the mean z_v to be 18 and 15.2 cm when based on z and z_c respectively, but found that these values were within one standard deviation (3.4 cm) of one another. Given the small difference in the mean z_v, we simply use $z_v = 15$ cm.

A comparison of the depth of the leading edge to the depth of the centroid for all type-S cases is made in figure 10 to obtain a relationship between z and z_c that will be useful later. Figure 10 suggests that $z_c + 15 = 0.83(z + 15)$. From the definition of

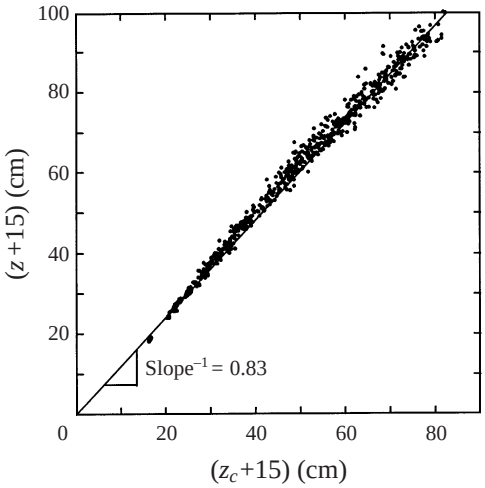

FIGURE 10. Comparison of depth of leading edge with depth of centroid for all 67 type-S cases.

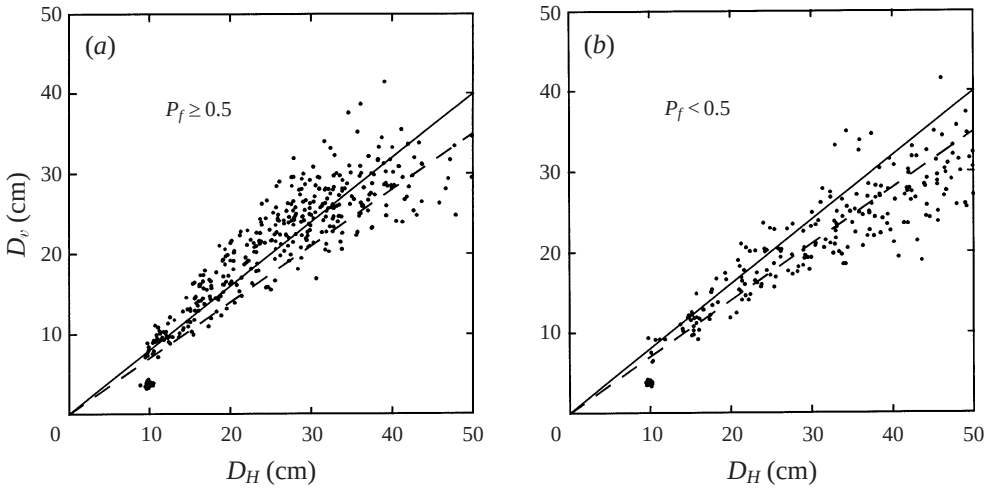

FIGURE 11. Vertical dimension versus horizontal dimension for high-P_f. (*a*) and low-P_f (*b*) type-S cases; dashed and solid lines correspond to $D_V/D_H = 0.7$ and 0.8, respectively.

l as the ratio of the vertical dimension of the thermal to its distance from the virtual origin ($l = D_V/(z + z_v)$), it may be shown that $z_c + z_v = (1 - l/2)(z + z_v)$, and thus, $l = 0.34$. Because of the small scatter of the points in figure 10, we conclude that z_c and z are equally useful parameters for characterizing a thermal's position. The billowy nature of thermals does not appear to result in excessive scatter when using the leading edge to define the thermal's position. Visual observations suggested that the particular shape of a thermal, including specific protrusions, is established quite early and is closely maintained as the thermal grows; this is consistent with the small scatter displayed in figure 10 and with Scorer's (1957) results.

The shape of a thermal may be approximated by an oblate spheroid which is characterized by D_V/D_H, where D_V and D_H are the vertical and lateral dimensions of the thermal. Estimates of D_V/D_H are necessary to predict the thermal volume below and are obtained here in two ways. In the first, we find D_V/D_H from plots of D_V

Case	$\bar{n}_1$	$\bar{n}_c$	Estimated D_V/D_H #1	Estimated D_V/D_H #2[c]	Predicted β_c #1	Predicted β_c #2	Observed β_c
$S, P_f < 0.5$	4.07	2.95	0.63[a]	0.69	0.100	0.110	0.090
N	4.10	3.44	0.70[b]	0.70	0.072	0.072	0.058
$S, P_f \geqslant 0.5$	5.15	3.95	0.80[a]	0.88	0.054	0.060	0.058

TABLE 4. Variation of mean parameters for type-N and type-S environments. [a] From figure 11, [b] from Turner (1964), [c] from $D_V/D_H = 0.17\,\bar{n}_1$.

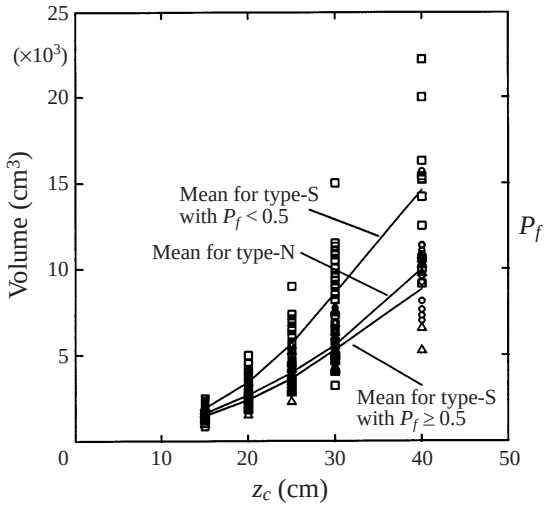

FIGURE 12. Measured volumes of thermals at selected depths, including all releases into type-S and 150 cm³ releases into type-N environments. △, type-S with $P_f \geqslant 0.5$; □, type-S with $P_f < 0.5$; ○, type-N.

versus D_H as given in figure 11, which shows a clear difference between the low- and high-P_f type-S cases. For $P_f \geqslant 0.5$ (figure 11*a*), the data exhibit an approximately linear variation of D_V with D_H and a mean D_V/D_H of 0.8 (solid line). This D_V/D_H is greater than the value for a neutral environment ($D_V/D_H \simeq 0.7$, dashed line), as deduced by Turner (1964) using Richards' (1961) and Scorer's (1957) data. For $P_f < 0.5$ (figure 11*b*), the data approximately match the neutral behaviour (dashed line) or perhaps $D_V/D_H \sim 0.75$ for small depths (where $D_H \leqslant 30$ cm), but on average fall below the neutral value for $D_H > 30$ cm. An approximate mean D_V/D_H over the entire data range is 0.63. Hence, with insufficient buoyancy to penetrate the density interface, the low-P_f thermals are squashed as z_c approaches z_1. In contrast, the D_V for the high-P_f cases appears to be unaffected on average by the density jump as the thermal approaches and passes through the jump. Moreover, the mean D_V/D_H exceeds that for the neutral environment.

A second D_V/D_H estimate can be obtained using the $\bar{n}_1$ values from tables 1 and 3 and the mean $l = D_V/(z + z_v)$ from figure 10, which exhibits little scatter. Since $\bar{n}_1 = (z + z_v)/r = 2(z + z_v)/D_H$, we have $D_V/D_H = l\bar{n}_1/2 = 0.17\,\bar{n}_1$. Table 4 compares this D_V/D_H (method 2) with that from method 1 and shows that the two are within 10% of one another; for the type-N cases, the estimates are identical.

The volume of each thermal was determined when its centroid was at specific depths

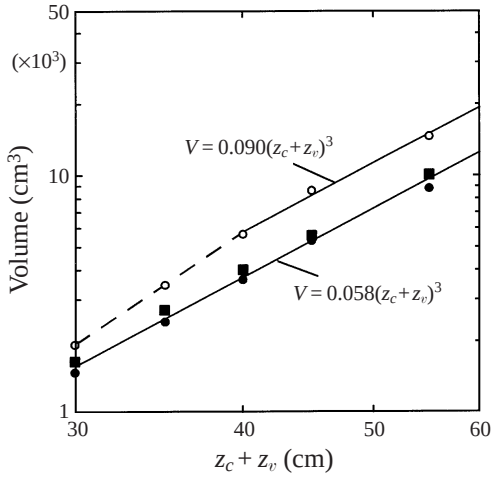

FIGURE 13. Average measured volumes for all releases into type-S and 150 cm^3 releases into type-N environments. •, type-S with $P_f \geqslant 0.5$; ○, type-S wtih $P_f < 0.5$; ■, type-N with 150 cm^3 releases.

(15, 20, 25, 30 and 40 cm) by using hand-drawn curves through individual plots of volume versus z_c. The values obtained are shown as a function of z_c in figure 12, where the lines are drawn through the mean for each type. Only positions before the thermal's centroid reached the interface were used. For some weak thermals that did not substantially penetrate the interface, the volume was observed to increase more rapidly than those that easily penetrated, consistent with the n_1 and D_V/D_H variation with P_f (figures 8 and 11). Based on the n_1 analysis, we present the volume data in three groups: type-S experiments with $P_f < 0.5$, type-S experiments with $P_f \geqslant 0.5$, and type-N experiments with 150 cm^3 releases. Figure 12 shows that the results for type-S with $P_f \geqslant 0.5$ fall close to the type-N results, whereas the type-S cases with $P_f < 0.5$ have somewhat larger volumes.

The mean observed volumes as a function of depth are plotted on logarithmic axes in figure 13 to determine a cubic fit to the data. The line $V = \beta_c(z_c + z_v)^3 = 0.058(z_c + z_v)^3$ is seen to be a good approximation to the type-N and high-P_f type-S cases. For low P_f, the β_c increases with depth until $z_c + z_v = 40$ cm (dashed line) and then remains constant with $V = 0.090(z_c + z_v)^3$ (solid line). The increase in β_c with depth is due to the density interface, the thermal's inability to penetrate it, and the change in the thermal geometry as a result (figure 11*b*).

A predicted volume can be expressed by $V_p = \beta_{cp}(z_c + z_v)^3$, where $\beta_{cp} = (4\pi/3)(D_V/D_H)/\overline{n}_c^3$. Table 4 presents the β_{cp} based on the estimates and $\overline{n}_c$ values and compares them to the observed β_c. The comparison shows that the predictions are within about 20% of the observations and that they are in closest agreement for the high-P_f cases. The differences between β_{cp} and the observed β_c for the low-P_f and type-N cases could be due to: (i) errors and/or uncertainty in the mean D_V/D_H, (ii) random variability in n_c and D_V/D_H, and (iii) for type-S, variations in the mean D_V/D_H and $\overline{n}_c$ with depth, especially near z_1. We note that for low P_f, the prediction would decrease to $\beta_{cp} = 0.091$ if we use a D_V/D_H (= 0.56) more representative of the late stage of the thermal, i.e. when it is clearly confined and distorted by the density jump (figure 11*b* for $D_H \geqslant 30$ cm). The latter β_{cp} is in excellent agreement with the observed β_c(= 0.090).

The above predictions and discussion show the importance of D_V/D_H, $\overline{n}_c$, and

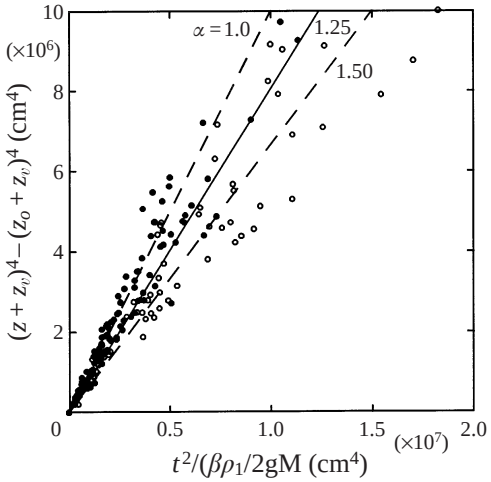

FIGURE 14. Fourth power of depth versus scaled square of time for all type-S cases compared with equation (3.6) for the determination of α; $\beta = 0.033$ is used for all data. •, $P_f \geqslant 0.5$; ○, $P_f < 0.5$.

related parameters in determining the thermal volume as well as the sensitivity of V_p to the former. Table 4 presents a natural ordering of the results showing how the density interface can have either a negative (low P_f) or positive (high P_f) effect on the entrainment coefficients ($\overline{n}_1, \overline{n}_c$) and D_V/D_H relative to the parameters for a neutral (type-N) environment. At first sight, a perplexing result is that the $\overline{n}_1$ values for the low-P_f and type-N cases agree whereas the $\overline{n}_c$ values differ. However, the differences in the $\overline{n}_1$ and $\overline{n}_c$ for the two cases are within their respective standard deviations. In addition, one might believe that the type-N parameters should agree better with the high-P_f results (as the volumes do) because type-N is, in a sense, an *infinitely strong* thermal since the interfacial jump is zero; but this is not observed. Further studies are necessary to explain the $\overline{n}_1$, $\overline{n}_c$, and D_V/D_H variation with P_f in terms of the thermal dynamics and overlying stratification.

An expression for the thermal volume as a function of the depth of the leading edge z can be obtained from the relationship between z and z_c [$z_c + z_v = 0.83(z + z_v)$] and that determined earlier between β and β_c. From $V = \beta(z+z_v)^3 = 0.058[0.83(z+z_v)]^3 = 0.033(z + z_v)^3$, we have $\beta = 0.033$ for the type-N and high-P_f type-S cases. The depth to the leading edge can be predicted from equation (3.6), given α, the virtual mass coefficient. To determine α, we can use equation (3.6), with $W_o = 0$ (our thermal starts from rest at $t = 0$), to get $(z + z_v)^4 - (z_o + z_v)^4 = [t^2/(\beta\rho_1/2gM)]/\alpha$. Our data are shown in figure 14 plotted as the left-hand side of this equation against the term in brackets on the right-hand side. Because equation (3.6) was derived for and strictly applies only in the neutral layer, only observations of thermals with depth less than the interface depth were included in figure 14. Lines are drawn for $\alpha = 1.0$, 1.25, and 1.50. The line for $\alpha = 1.25$ is seen to be a reasonable fit to the data and this value should be used in equation (3.6).

Richards (1961) established an empirical expression for the fraction of a thermal that penetrates a step-change interface. He defined a parameter $S = V(\rho_2 - \rho_1)/M$ as a measure of the strength of the density difference compared with the buoyancy of the thermal as it straddled the interface. V is the measured volume of the thermal when its widest span is at the interface. Richards found that the fraction of the thermal that penetrated the interface decreased linearly as S increased from 0 to 1.9, with no

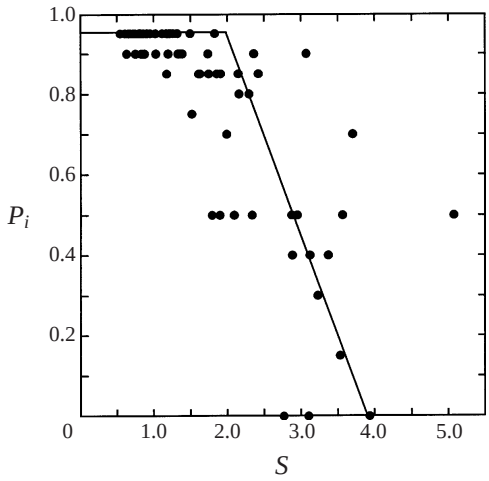

FIGURE 15. Initial penetration versus Richards' S (uses measured volume).

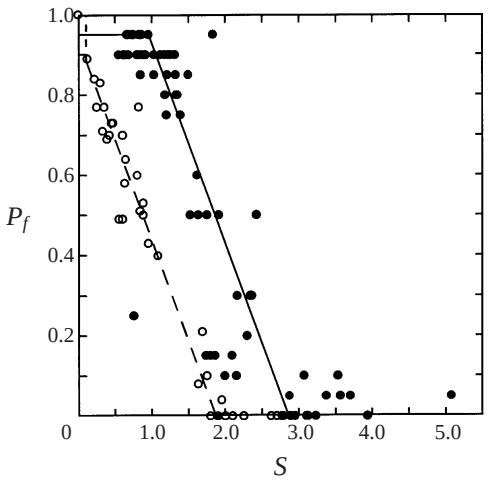

FIGURE 16. Final penetration versus Richards' S (uses measured volume). Open symbols and dashed line are from Richards (1961); solid symbols are current data.

penetration above $S = 1.9$. For the current experiments, we used plots of the observed volume versus z_c to determine V when the centroid was at the interface. Observations of the initial penetration are shown as a function of S in figure 15. The largest P_i was 0.95 because approximately 5% of each thermal was estimated to remain in a *tail* that formed behind the thermal (cf. figure 2). A simple hand-drawn approximation to P_i, as shown by the line in figure 15, may be written

$$P_i = \begin{cases} 0.95, & S < 2 \\ 0.5(3.9 - S), & 2 \leqslant S \leqslant 3.9 \\ 0, & 3.9 < S. \end{cases}$$

For most thermals, some of what initially penetrated the interface returned to the interface as discussed earlier, and thus it is more useful to consider the final penetration. Final penetration is shown plotted against S in figure 16, and on average,

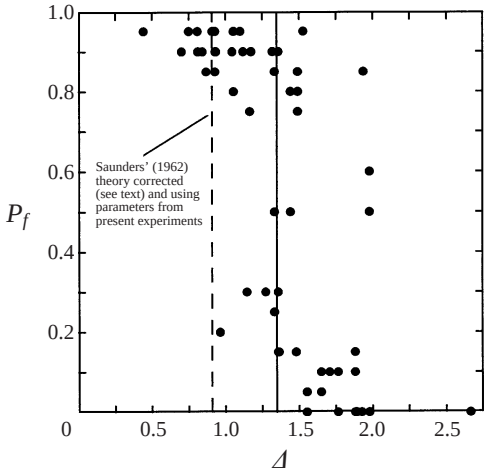

FIGURE 17. Final penetration versus Δ.

it is seen to be much less than the initial penetration at a given S. A simple approximation for the final penetration, as shown by the solid line in figure 16, is

$$P_f = \begin{cases} 0.95, & S < 1 \\ 0.5(2.9 - S), & 2 \leqslant S \leqslant 2.9 \\ 0, & 2.9 < S. \end{cases}$$

Richards' (1961) observations were of final penetration and his results are included in this figure (as open symbols). His approximation, shown as the dashed line, is

$$P_f(\text{Richards}) = \begin{cases} 1.00, & S < 0.1 \\ 0.5(1.9 - S), & 0.1 \leqslant S \leqslant 1.9 \\ 0, & 1.9 < S. \end{cases}$$

Note that our line is parallel to Richards' but is shifted to larger S. On physical grounds, we have difficulty accepting his results. For example, consider a thermal falling through a layer of fresh water into a fluid layer of higher density. This thermal approaches the interface with a value of S less than 1 and, thus, has an average density greater than that in the lower layer. Given this and its positive momentum, the thermal may be expected to continue falling, resulting in essentially total penetration. Our results are in better agreement with this argument than are Richards'; his results suggest a P_f of only 0.50 when $S = 0.9$.

We recommend use of the formula $V_p = 0.058(z_1 + z_v)^3$ to predict the volume of a thermal when its centroid is at the interface, and define a parameter $\Delta = 0.058(z_1 + z_v)^3(\rho_2 - \rho_1)/M$. We use this parameter to predict the penetration *a priori*. Final penetration is plotted against Δ in figure 17, where as a simple approximation for prediction, the line $\Delta = 1.35$ is used to divide the data into either total or no penetration of the interface. Saunders' theory, as described above, predicts total penetration when $\gamma(\mu^2 - 1) < 1$. Using our empirical results (namely, $\beta = 0.033$ and $l = 0.34$), his expression may be reworked to show that total penetration occurs when $\Delta < 0.92$. This value is shown as the dashed line in figure 17 and is seen to underestimate the penetration capability of a thermal in our experiments. On the other hand, Saunder's prediction using our empirical results is a conservative estimate

Case	z_1 (cm)	$d\rho/dz \times 10^4$ (g cm^{-4})	M (g)	P_T	z_{mx} (cm)	z_{eq} (cm)	σ_z (cm)	$\frac{z_{mx}-z_1}{z_1+z_v}$	$\frac{z_{eq}-z_1}{z_1+z_v}$	$\frac{\sigma_z}{z_1+z_v}$	Mass check
28	30	1.1	14.7	0.42	75	49.8	7.6	1.00	0.44	0.17	1.06
29	30	1.1	14.7	0.42	80	52.4	8.2	1.11	0.50	0.18	1.11
30	30	1.1	14.7	0.42	75	51.6	7.8	1.00	0.48	0.17	1.08
31	30	1.1	14.7	0.42	70	48.3	6.3	0.89	0.41	0.14	1.22
55	32	3.6	29.6	0.36	55	44.7	3.5	0.49	0.27	0.07	0.95
56	32	3.6	29.6	0.36	55	42.6	3.5	0.49	0.23	0.07	0.95
57	32	3.6	29.6	0.36	60	44.4	4.2	0.60	0.26	0.09	1.08
58	32	3.6	29.6	0.36	65	47.0	4.1	0.70	0.32	0.09	1.08
59	32	3.6	29.6	0.36	65	49.0	3.8	0.70	0.36	0.08	0.93
60	32	3.6	29.6	0.36	55	44.0	3.4	0.49	0.26	0.07	0.89
61	32	3.6	29.6	0.36	65	42.3	3.4	0.70	0.22	0.07	0.99
62	32	3.6	29.6	0.36	65	48.6	3.7	0.70	0.35	0.08	0.97
109	49	1.1	5.3	0.23	65	53.5	2.8	0.25	0.07	0.04	1.42
110	49	1.1	5.3	0.23	65	53.8	2.9	0.25	0.07	0.05	1.20
111	49	1.1	5.3	0.23	70	54.6	3.8	0.33	0.09	0.06	1.33

TABLE 5. Samples of test conditions and observations for type-G environments. A complete table showing all cases is available from the JFM Editorial Office.

of complete or no penetration in that only near complete penetration do data fall to the left of the dashed line. For the solid line, four points with $P_f \leqslant 0.5$ lie to the left of the solid line and therefore the empirical estimate of $\Delta = 1.35$ grossly overpredicts the penetration capability for these four cases.

4.3. *Type-G and type-SG environments*

When released into a neutral layer followed by a constant-density-gradient region, a thermal will move only a finite distance before coming to rest with $z = z_{mx}$. The thermal's momentum will result in an overshoot of the equilibrium position to one where the buoyancy is negative; the thermal will then move back toward the neutral layer. It will eventually come to rest with its centroid at an equilibrium height z_{eq}. As discussed in § 3, the thermal may or may not completely enter the gradient layer before coming to rest. The range of experiments conducted here included both situations. In addition to several experiments with a type-G environment, two experiments were conducted with a type-SG environment.

Twelve sets of experiments were conducted with a type-G environment; the initial conditions and selected results are listed in table 5. All but one set (of four repetitions) consisted of six to eight repetitions. Within these twelve sets z_1 was varied from 19 to 49 cm, $d\rho/dz$ was nominally 0.0001 or 0.0004 g cm^{-4}, and M was varied from 5.0 to 35 g. The total volume of each release was 150 cm^3, of which 75 cm^3 was blue dye.

For each experiment, z_{mx} was observed and recorded. Just after the thermal reached its equilibrium depth, the sample rake was towed through it. The measured dye concentrations were used to compute the mass of dye in the horizontal layer corresponding to each horizontal group of ten sampling ports. Examples of the vertical distribution of dye for eight repetitions of an experiment are shown in figure 18. These distributions were used to compute the vertical position of the centroid (centre of mass) and the vertical spread (expressed as the standard deviation of the mass distribution) for each experiment. A check on the integrity of this method was made by summing the masses of dye in the layers and calculating the ratio of this sum to the mass of

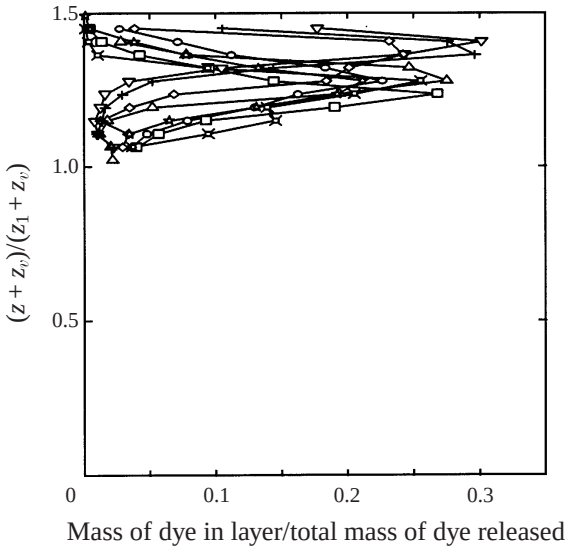

FIGURE 18. Vertical distribution of tracer (dye, by volume) for eight type-G cases (nos. 55–62).

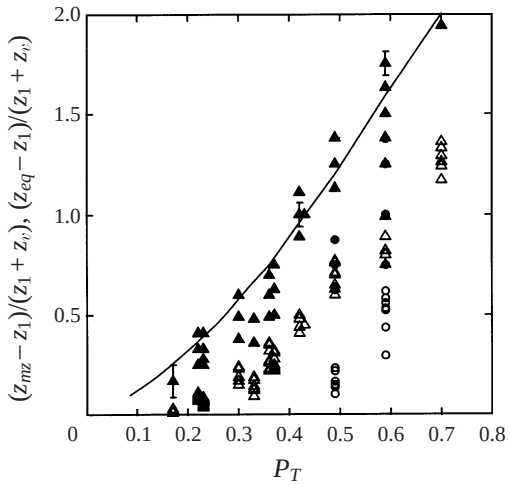

FIGURE 19. Maximum penetration depth beyond the interface (solid symbols) and equilibrium depth of centroid (open symbols) for type-G and type-SG experiments. Line is Saunders' (1962) theory for maximum penetration for type-G environment. ▲, △, type-G; ●, ○, type-SG. Sample error bars indicate typical grid resolution (±2.5 cm).

dye released; ideally, the ratio should be 1. This *mass continuity check*, as listed in the last column of table 5 for all 84 releases, had a mean value of 1.06 and standard deviation of 0.11, which is regarded as quite good considering the coarse spacing of the sampling ports.

The observed maximum penetration depths for all experiments are plotted against P_T in figure 19. For the type-G experiments (solid squares and triangles), Saunders' theoretical prediction (using our empirical values for β and l) was used to obtain the solid line that is seen to be a good fit to the observations. The equilibrium depths (open symbols) are also shown in figure 19. There is no theoretical prediction for

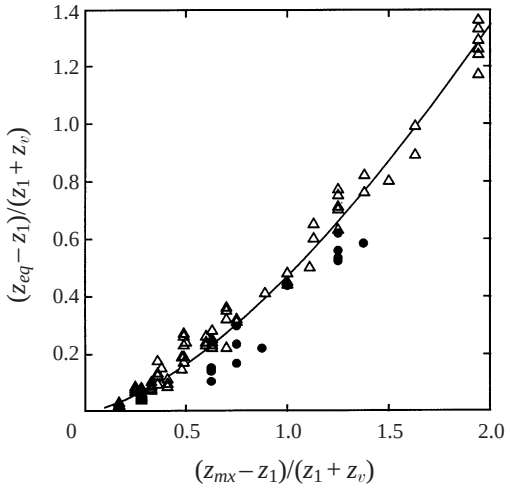

FIGURE 20. Equillibrium depth of centroid compared with maximum penetration depth: △, type-G; •, type-SG.

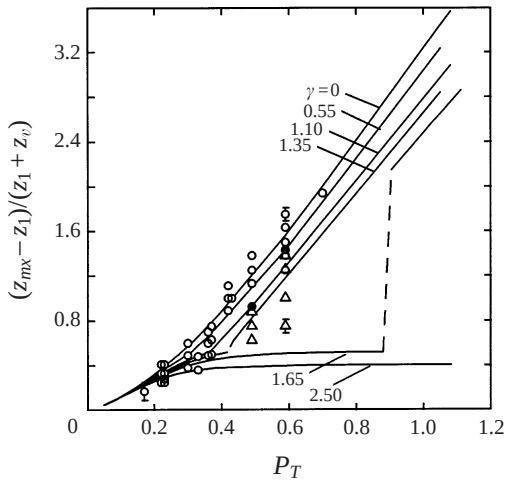

FIGURE 21. Maximum penetration depth beyond the interface for type-SG and type-G experiments: ○, type-G observation; △, type-SG observation; •, type-SG predictions. Lines are theoretical predictions for values of γ as specified. Sample error bars indicate typical grid resolution (± 2.5 cm).

the equilibrium depth, but as seen in figure 20, z_{eq} is related to z_{mx} and can be approximated by the formula $(z_{eq}-z_1)/(z_1+z_v) = 0.47[(z_{mx}-z_1)/(z_1+z_v)]^{1.52}$. (This formula is applicable only over the range shown.)

Two experiments (with seven repetitions of each) were conducted with a type-SG environment. The density profile for these experiments was shown in figure 1, and the initial conditions and selected results are listed in table 6. According to the theoretical arguments presented in § 3, the thermal should completely penetrate the interface before reversing direction at z_{mx} for both cases ($P_T = 0.49$ with $\gamma = 1.13$ and $P_T = 0.59$ with $\gamma = 0.55$). The visual observations of the maximum depth of penetration are shown as the open triangles in figure 21 (only seven symbols appear, but fourteen realizations are represented; several had identical results. See table 6). Two non-dimensional parameters are required to characterize this situation: γ and P_T.

Case	(g)	P_T	γ	z_{mx}	z_{eq} (cm)	σ_z (cm)	$\frac{z_{mx}-z_1}{z_1+z_v}$ (cm)	$\frac{z_{eq}-z_1}{z_1+z_v}$	$\frac{\sigma_z}{z_1+z_v}$	Mass check
112	14.9	0.49	1.13	50	30.6	6.6	0.63	0.14	0.17	1.32
113	14.9	0.49	1.13	50	30.9	5.9	0.63	0.15	0.15	1.32
114	14.9	0.49	1.13	60	33.8	8.8	0.88	0.22	0.22	1.26
122	30.3	0.59	0.55	80	48.4	12.2	1.38	0.59	0.31	0.91
123	30.3	0.59	0.55	65	42.5	8.0	1.00	0.44	0.20	1.17
124	30.3	0.59	0.55	75	46.4	9.9	1.25	0.54	0.25	1.09
125	30.3	0.59	0.55	55	36.9	7.4	0.75	0.30	0.19	1.27

TABLE 6. Samples of test conditions and observations for type-SG environments. For all cases: $z_i = 25\,\text{cm}$, $\rho_2 - \rho_1 = 0.006\,\text{g cm}^{-3}$, and $\mathrm{d}\rho/\mathrm{d}z = 0.0001\,\text{g cm}^{-4}$. A complete table showing all cases is available from the JFM Editorial Office.

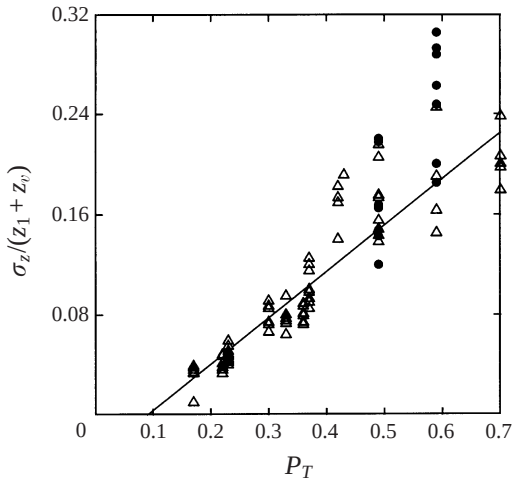

FIGURE 22. Vertical spread of thermals at equilibrium height as function of P_T: △, type-G; •, type-SG.

This figure was prepared using P_T as the abscissa and drawing lines corresponding to various values of γ. The theoretical predictions for the two sets of experimental conditions studied are shown on the figure as filled circles and are seen to serve as an upper bound for the observations. For completeness, the observations discussed earlier with no step change are also included (open symbols) and should be compared with the theoretical line $\gamma = 0$. The observations with a step change are somewhat below the line for cases with no step change, but additional measurements should be considered before drawing firm conclusions.

The vertical spread (standard deviation about the centroid) of the thermals just after reaching the equilibrium height is shown as a function of P_T in figure 22 and as a function of z_{mx} in figure 23. Hand-drawn lines are included on these figures, with the dashed line on figure 23 for the type-SG cases. Either P_T or z_{mx} could be used to predict the vertical spread for the type-G situations by using the solid line through the data in those figures. For the type-SG environment modelled here, however, the vertical spread is increased significantly and more experiments with varied values

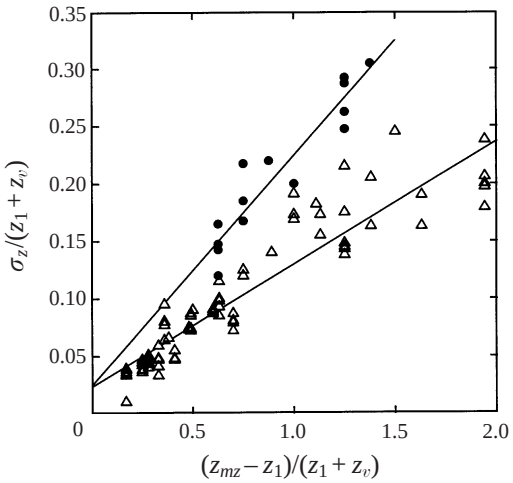

FIGURE 23. Vertical spread of thermals at equilibrium height as function of maximum penetration depth: △, type-G; •, type-SG.

of gradient and density difference at the base are needed to determine a prediction algorithm.

5. Summary

Open detonation is the most frequently used method of disposing of obsolete munitions. Current detonation activities are limited to the daytime CBL in order to maximize dispersion rates of the contaminant clouds and to minimize long-range transport of high-concentration clouds. Information on the behaviour of the thermal cloud and interaction with an elevated inversion is necessary for the development of cloud models.

Laboratory experiments were undertaken to investigate the rise and spread of buoyant thermals and their inversion penetration capability. The thermal rise was simulated by the descent of negatively buoyant fluid within a tank of quiescent water. The experimentally generated thermals descended either through a neutral environment (type-N) or a neutral layer of depth z_1 followed by a stably stratified region. The stable region consisted of: (i) a step change in density (type-S), (ii) a constant-gradient layer (type-G), or (iii) a combination of the above two (type-SG). These density structures simulate the variation in the potential temperature profiles capping the CBL and thus the types of conditions likely to be encountered by a full-scale detonation cloud.

For the neutral environment, the thermal growth was similar to that found by Scorer (1957) – a linear increase in the thermal horizontal dimension D_H with depth z. Specifically, $D_H = 2(z + z_v)/n_1$, where n_1 was approximately constant for a given thermal but exhibited less than 15% variability about its mean value n_1 of about 4 (groups 1 and 3, table 1). The $\overline{n}_1$ values for the low-penetration ($P_f < 0.5$) type-S cases was consistent with the above $\overline{n}_1$, and both neutral and low-P_f values were consistent with the $\overline{n}_1$ (= 3.84) found by Scorer. For the high-P_f type-S cases, $\overline{n}_1$ was somewhat larger (5.15), implying a slower entrainment rate. In contrast with these results, the thermal volume as a function of depth exhibited more consistency between the type-N and high-P_f type-S cases due to the variation in D_V/D_H with the

environment type (N and S) and P_f (table 4). The average observed volume for these cases (type-N, high-P_f type-S) was found to be $V = 0.058(z_c + z_v)^3$, and the predicted V based on the $\bar{n}_c$ and D_V/D_H agreed to within about 20% of the observed values. Similar agreement was found between the predicted and observed volumes for the low-P_f type-S cases.

Thermal penetration of the interface (type-S) was observed to decrease linearly with the dimensionless parameter $S = V(\rho_2 - \rho_1)/M$ as S increased from 1 to 2.9, where V is the observed volume when $z_c = z_1$. The qualitative behaviour of P_f versus S was similar to that found by Richards (1961) but occurred over a different S range (1 to 2.9) compared with Richards' (0.1 to 1.9). As a simplified procedure useful in applications, we developed a penetration criterion based on the average volume of penetrating thermals and a dimensionless parameter $\Delta = V_p(\rho_2 - \rho_1)/M$ where V_p is the predicted volume at the interface ($= 0.058(z_1 + z_v)^3$). A value of $\Delta = 1.35$ was generally found to separate the non-penetrating thermals ($\Delta > 1.35$) from the penetrating ones ($\Delta < 1.35$).

For the experiments with the elevated gradient layer (type-G), the observed maximum penetration depth z_{mx} agreed well with Saunders' (1962) theoretical prediction. In addition, the thermal equilibrium height and vertical spread exhibited a systematic dependence on z_{mx} and/or the parameter $P_T = (Mg/\rho_1)^{1/4}/[(z_1 + z_v)N^{1/2}]$. Limited experiments with a step change in density at the base of the constant-gradient layer (type-SG) showed that an extension of Saunders' theory was useful in predicting the maximum penetration distance. However, additional experiments are required to develop a prediction algorithm for the equilibrium depth and vertical spread.

The experimental results described in this paper and obtained in a quiescent environment are being used in the development of a dispersion model for open detonation clouds (Weil *et al.* 1996). The next step in the development is a series of experiments in the presence of ambient convectively generated turbulence, i.e. in a laboratory convection tank. Such experiments are in progress and will be reported in a future paper.

This research was partially funded by the US Department of Defense/Department of Energy/Environmental Protection Agency through the Strategic Environmental Research and Development Program. The National Center for Atmospheric Research is sponsored by the National Science Foundation. Mr Van Hursey (Geophex, Inc.) prepared the tank and release solutions and assisted greatly in the conduct of these experiments. Mr Len Marsh (Geophex, Inc.) performed the tedious video analysis that was required to quantify the results. Mr Michael Shipman (Geophex, Inc.) provided computer support in the data analysis. We acknowledge their help with gratitude.

The information in this document has been subjected to review within the Environmental Protection Agency and approved for publication. Mention of trade names or commercial products does not constitute endorsement or recommendation for use.

REFERENCES

Morton, B. R., Taylor, G. I. & Turner, J. S. 1956 Turbulent gravitational convection from maintained and instantaneous sources. *Proc. R. Soc. Lond.* A **234**, 1–23.

Perry, S. G. & Snyder, W. H. 1989 Laboratory simulation of daytime mixed layer heights in complex terrain. In *Preprint Vol., Sixth Joint Conf. on Appl. of Air Poll. Meteorology, Jan. 30–Feb. 3, 1989, Anaheim, CA,* pp. 256–259. Am. Met. Soc., Boston, MA.

Richards, J. M. 1961 Experiments on the penetration of an interface by buoyant thermals. *J. Fluid Mech.* **11**, 369–384.

Saunders, P. M. 1962 Penetrative convection in stably stratified fluids. *Tellus* **14**, 178–194.

Scorer, R. S. 1957 Experiments on convection of isolated masses of buoyant fluid. *J. Fluid Mech.* **2**, 583–594.

Snyder, W. H. 1981 Guideline for fluid modeling of atmospheric diffusion. *Rep.* EPA-600/8-81-001. US Environmental Protection Agency, Research Triangle Park, NC., 186p.

Thompson, R. S. & Snyder, W. H. 1976 EPA Fluid Modeling Facility. In *Proc. Conf. on Modeling and Simulation*, Rep. EPA-600/9-76-016. 488–492. US Environmental Protection Agency, Washington, DC., July.

Thompson, R. S. & Snyder, W. H. 1996*a* Laboratory simulation of the rise of buoyant thermals created by open burning and detonation – Part I: neutral layer and step inversion. Project Data Report. Fluid Modeling Facility, US Environmental Protection Agency, Research Triangle Park, NC., 48p.

Thompson, R. S. & Snyder, W. H. 1996*b* Laboratory simulation of the rise of buoyant thermals created by open burning and detonation - Part II: elevated gradient and step inversion with elevated gradient. Project Data Report. Fluid Modeling Facility, US Environmental Protection Agency, Reasearch Triangle Park, NC., 38p.

Turner, J. S. 1957 Buoyant vortex rings. *Proc. R. Soc. Lond.* A **239**, 61–75.

Turner, J. S. 1964 The dynamics of spheroidal masses of buoyant fluid. *J. Fluid Mech.* **19**, 481–490.

Turner, J. S. 1986 Turbulent entrainment: the development of the entrainment assumption, and its application to geophysical flows. *J. Fluid Mech.* **173**, 431–471.

Weil, J. C., Templeman, B. T., Banta, R. & Mitchell, W. J. 1996 Dispersion model development for open burn/open detonation sources. In *Preprint Vol., Ninth Joint Conf. on Appl. of Air Poll. Meteorology*, pp. 610–616. Am. Metr. Soc., Boston, MA.

Wyngaard, J. C. 1988 Structure of the PBL. In *Lectures on Air Pollution Modeling* (ed. A. Venkatram & J. C. Wyngaard), pp. 9–61. Am. Met. Soc., Boston, MA.